CMS Physics Analysis Summary

Contact: cms-pag-conveners-exotica@cern.ch 2018/03/12

Search for dark matter in association with a $t\bar{t}$ pair at $\sqrt{s} = 13$ TeV in the dilepton channel with 2016 data

The CMS Collaboration

Abstract

A search is performed for dark matter produced in association with $t\bar{t}$ pairs in data from proton-proton collisions at a center-of-mass energy of 13 TeV at the LHC. The data corresponds to 35.9 fb^{-1} collected with the CMS detector in 2016. The analysis looks for an excess of events with large imbalance in transverse momentum and a top quark pair decaying in the dileptonic mode. The results are interpreted in the context of simplified models of dark matter production. Assuming unitary coupling values to standard model (SM) particles g_q, and dark matter (DM) particles g_χ, and DM mass $m_\chi = 1$ GeV, the observed (expected) 95% CL exclusions for a scalar mediator are $m_\phi < 74\,(99)$ GeV. The 95% CL exclusion expected for a pseudoscalar mediator is $m_a < 50$ GeV, while none is observed.

1 Introduction

Initially postulated by F. Zwicky [1], the existence of dark matter (DM) is strongly supported by indirect evidence from astrophysical observations, such as galactic rotation velocity dispersion curves [2] and gravitational lensing from cluster mass measurements [3]. The standard model (SM) does not predict the nature of DM nor of the forces governing SM-DM interactions. The possibility remains open that DM interacts with ordinary matter via forces besides gravity. Compelling extensions to the SM aiming at circumventing the hierarchy problem [4–6] postulate the existence of new, stable, weakly interacting particles at the electroweak scale ($\sim$ 100 GeV), so-called WIMPs [7]. The typical WIMP annihilation cross sections would lead to the observed DM relic abundance from the freeze-out mechanism, known as the "WIMP miracle". Consequently, the LHC provides a rich playground for the direct production and detection of DM by all-purpose detectors such as CMS and ATLAS. If DM particles are produced, they would escape the detector undetected, creating an imbalance of momentum in the plane transverse to the beams ($\vec{p}_{\mathrm{T}}^{\,\mathrm{miss}}$).

The Minimal Flavor Violation (MFV) [8, 9] hypothesis is strongly motivated by the apparent lack of new flavor physics at the electroweak scale. If the new physics associated with DM obeys the principle of MFV, then mediator interactions inherit the Yukawa structure of the SM. In this scenario, the coupling of DM to heavy flavors such as the top quark is favored. At leading order, the process is gluon-induced and a $\mathrm{t\bar{t}}$ pair is produced in association with a pair of DM fermions, as shown in Fig. 1. The DM fermions can be either Dirac or Majorana with the difference being a factor of two in the cross section; they are taken to be Dirac fermions in the following.

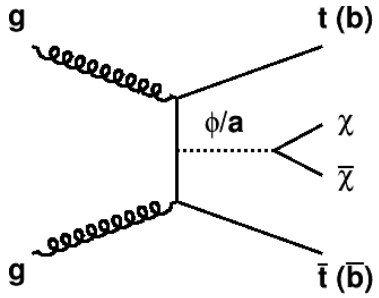

Figure 1: Leading order Feynman diagram describing the production of DM particles (χ) in association with a top (bottom) quark pair through a spin-0 mediator (ϕ/a).

This note describes a search for DM in the $\mathrm{t\bar{t}}$ dilepton final state, in which both W bosons from the top quarks decay into a lepton and the corresponding neutrino. Three strategies that analyze the proton-proton (pp) collision data collected by the CMS detector in 2016 at $\sqrt{s} = 13$ TeV are presented. One strategy exploits the increased $\vec{p}_{\mathrm{T}}^{\,\mathrm{miss}}$ due to the undetected DM particles in a possible signal scenario. The other two strategies follow multi-variate analysis (MVA) approaches and rely on the kinematic reconstruction of the $\mathrm{t\bar{t}}$ system, detailed in Sec. 5. The MVA strategies exploit differences in the $\mathrm{t\bar{t}}$ reconstruction between SM processes and the possible signal. An artificial neural network (ANN) trained on a discriminator which estimates the potential signal mediator p_{T} is used in one of the MVA strategies. Another MVA strategy employs a boosted decision tree (BDT) method to explore top quark spin correlation modifications through the radiation of the DM mediator.

The interpretation of searches for DM in these and other channels at the LHC assume simplified DM models, which are most appropriate when considering DM mediator production spanning a broad range of mediator and DM particle masses. Spin-0 mediators with pure scalar or pseu-

doscalar couplings are assumed. The simplified model scheme employed in this analysis is consistent with the recommendations of the LHC Dark Matter Forum [10–12] where the free parameters are the masses of the DM particle (m_χ) and mediator (m_ϕ), the coupling strength of the mediator to fermions (g_q) and the coupling of the mediator to the DM particles (g_χ).

2 Signal and background modeling

Monte Carlo (MC) simulation events are employed to model the expected signal and background processes. Several different generators are used in the simulation.
MADGRAPH5_AMC@NLO (v5.2.3.3) [13], including MADSPIN [14], is used to generate $t\bar{t}$ +DM signal events with at most one additional parton from initial state radiation at leading-order (LO) accuracy, where the MLM scheme [15] is applied to merge the different parton multiplicities. Yukawa couplings ($g_{SM} = g_q m_q / v$, where m_q denotes the quark mass and v is the vacuum expectation value) between the mediator and SM quarks are assumed in these signal models. Additionally, the coupling constant g_q is set to unity and assumed to be flavor-universal. The DM particle itself is taken to be a Dirac fermion and its coupling to the mediator, g_χ, is also set to unity for all interpretations shown. The formulae used to calculate the minimum mediator widths are given in [16]. The NNPDF3.0 [17] parton distribution functions (PDFs) are utilized as default in the MC calculations for all generated samples. Fragmentation, hadronization and underlying events are simulated using PYTHIA (v8.2) [18, 19] and the CUETP8M1 tune [20, 21]. For the dilepton channel $t\bar{t}$ decay, exclusive samples are employed whereas for the semileptonic and fully hadronic channels, inclusive samples are used. Table 1 summarizes the generated mediator and dark matter mass points as well as the corresponding cross sections at next-to-leading order, which are used for normalization.

Table 1: Summary of the signal MC samples and their corresponding NLO cross sections as used in this analysis. $m_\chi = 1$ GeV is assumed in all samples. Left column: mass of the mediators; central: scalar mediator case; right: pseudoscalar mediator case.

m_ϕ (GeV)	S NLO cross section (pb)	PS NLO cross section (pb)
10	26.09	0.6218
20	13.96	0.5653
50	3.923	0.4314
100	0.8891	0.2716
200	0.1229	0.1189
300	0.04079	0.05946
500	0.007796	0.008171

Background contributions from $t\bar{t}$, associated $t\bar{t}$ production with an additional Z/W boson, single top-quark events, Drell–Yan background (i.e. quark-antiquark annihilation into lepton-antilepton pairs through virtual photon or Z boson exchange), single W boson and diboson events (WW, WZ, and ZZ) with multiple jets are taken from MC simulations and corrected either with a data-driven approach or by scaling with the most precise available theory prediction.

The next-to-leading-order (NLO) POWHEG (v2) [22, 23] generator is employed to generate $t\bar{t}$ background events, assuming a top quark mass of $m_t = 172.5$ GeV. The events are interfaced to PYTHIA (v8.2) for fragmentation, hadronization and to simulate the underlying event using the recently determined CUETP8M2T4 tune [24]. Finally, the events are normalized to the theoretical $t\bar{t}$ cross section calculated at next-to-next-to-leading order (NNLO) in perturbative

QCD, including soft-gluon resummation at next-to-next-to-leading-log order (NNLL) [25–30].

The $t\bar{t}Z$ and $t\bar{t}W$ background samples as well as the contribution from single boson production, Z/W with multiple jets, were generated using MADGRAPH5_AMC@NLO (v5.2.2.2). $t\bar{t}Z$ and $t\bar{t}W$ events are generated at NLO applying MC@NLO [31] merging. For single boson production, up to four additional partons were added at LO and the MLM matching scheme are used to combine the different parton multiplicities. The generation of Drell–Yan events is split into two distinct invariant mass ranges: $10 - 50$ GeV and > 50 GeV.

Single top quark production is generated at NLO and normalized to the approximate NNLO cross section [32]. While W boson associated single top production was simulated using POWHEG (v1) [33], t-channel single top production was generated using POWHEG (v2) and MADSPIN. As for $t\bar{t}$ production, the CUETP8M2T4 tune is applied. Diboson production (WW, WZ, and ZZ) is simulated with LO accuracy using PYTHIA (v8.2) and the CUETP8M1 tune, and normalized to their NLO cross sections [34].

The detector response is simulated with the GEANT4 program [35]. PYTHIA (v8.2) [18, 19] is used to simulate pileup events, which are additional interactions per bunch crossing. All samples are reweighted to match the luminosity profile observed in data.

3 The CMS detector

The central feature of the CMS apparatus is a superconducting solenoid of 6 m internal diameter, providing a magnetic field of 3.8 T. Within the solenoid volume are a silicon pixel and strip tracker, a lead tungstate crystal electromagnetic calorimeter (ECAL), and a brass and scintillator hadron calorimeter (HCAL), each composed of a barrel and two endcap sections. Forward calorimeters extend the pseudorapidity coverage provided by the barrel and endcap detectors. Muons are detected in gas-ionization chambers embedded in the steel flux-return yoke outside the solenoid, with detection planes made using three technologies: drift tubes, cathode strip chambers, and resistive plate chambers.

The particle-flow event algorithm [36] reconstructs and identifies each individual particle with an optimized combination of information from the various elements of the CMS detector. The energy of photons is directly obtained from the ECAL measurement, corrected for zero-suppression effects. The energy of electrons is determined from a combination of the electron momentum at the primary interaction vertex as determined by the tracker, the energy of the corresponding ECAL cluster, and the energy sum of all bremsstrahlung photons spatially compatible with originating from the electron track. The energy of muons is obtained from the curvature of the corresponding track. The energy of charged hadrons is determined from a combination of their momentum measured in the tracker and the matching ECAL and HCAL energy deposits, corrected for zero-suppression effects and for the response function of the calorimeters to hadronic showers. Finally, the energy of neutral hadrons is obtained from the corresponding corrected ECAL and HCAL energy. Jet momentum is determined as the vectorial sum of all particle momenta in the jet, and is found from simulation to be within 5 to 10% of the true momentum over the whole p_T spectrum and detector acceptance. An offset correction is applied to jet energies to take into account the contribution from additional proton-proton interactions within the same or nearby bunch crossings. Jet energy corrections are derived from simulation, and are confirmed with in situ measurements of the energy balance in dijet and photon + jet events [37]. Additional selection criteria are applied to each event to remove spurious jet-like features originating from isolated noise patterns in certain HCAL regions. The momentum resolution for electrons with $p_T \approx 45$ GeV from $Z \to ee$ decays ranges from 1.7%

for nonshowering electrons in the barrel region to 4.5% for showering electrons in the endcaps [38]. Muons are measured in the pseudorapidity range $|\eta| < 2.4$. Matching muons to tracks measured in the silicon tracker results in a relative transverse momentum resolution for muons with $20 < p_T < 100\,\text{GeV}$ of 1.3–2.0% in the barrel and better than 6% in the endcaps, The p_T resolution in the barrel is better than 10% for muons with p_T up to 1 TeV [39].

A more detailed description of the CMS detector, together with a definition of the coordinate system used and the relevant kinematic variables, can be found in Ref. [40].

4 Event selection

Signal events contain a pair of non-interacting DM particles and a pair of top quarks. Large p_T^{miss} (magnitude of $\vec{p}_T^{miss}$) is expected to manifest from the production of the DM particles, and the top quark decays proceed via on-shell W boson decays to lepton-neutrino pairs.

The data used for this analysis are collected using a combination of triggers designed to record events containing either one or two high-p_T leptons passing isolation and identification criteria. Double lepton triggers include a dimuon trigger requiring two muons satisfying $p_T > 17$ GeV and $p_T > 8$ GeV, a dielectron trigger requiring two electrons satisfying $p_T > 23$ GeV and $p_T > 12$ GeV, and muon-electron triggers requiring a muon with $p_T > 8$ GeV (23 GeV) and an electron with $p_T > 23$ GeV (12 GeV). Single lepton triggers include an electron trigger requiring $p_T > 27$ GeV and a muon trigger requiring $p_T > 24$ GeV. The overall trigger efficiency is ensured to be greater than 90% in the analysis once offline p_T and tight lepton requirements are applied.

In this document, three strategies targeting a dilepton final state with additional p_T^{miss} are presented, where signal extraction is performed by fitting the shapes of three different observables: p_T^{miss}, a BDT discriminant, and an ANN discriminant. The strategies are described in greater detail in Sec. 6, but the event selection requirements are, in large part, common to all three. Events with $p_T^{miss} > 50$ GeV, two or more jets of which at least one is b-tagged, and exactly two leptons passing tight isolation and identification criteria are selected. Jets are required to have a p_T above 30 GeV and $|\eta| < 2.4$. The Combined Secondary Vertex (CSVv2) b-tagging algorithm [41] is used to identify jets originating from bottom quark hadronization. Jets are considered b-tagged if the jet CSVv2 discriminant passes the medium working point requirement (CSVv2M). This corresponds to efficiencies of 69% to tag b jets, 35% to tag c jets, and 1% to misidentify light-flavor jets. The leading lepton is required to have $p_T > 25$ GeV and the trailing lepton is required to have at least $p_T > 15$ GeV. Furthermore, the event must not have any additional leptons satisfying loose lepton requirements with $p_T > 10$ GeV. Same flavor events (ee and $\mu\mu$) must have a dilepton mass at least 15 GeV away from the Z boson pole mass (M_Z) in order to reduce the large background from dilepton decays of Z bosons. In order to reduce backgrounds from low-mass dilepton resonances (e.g. J/ψ, Y) and Drell-Yan (DY), the dilepton mass of all events is required to be greater than 20 GeV.

5 Kinematic reconstruction of the $t\bar{t}$ system

A quantity estimating how closely the measured final state corresponds to a $t\bar{t}$ rather than a $t\bar{t}$ plus additional p_T^{miss}topology is extracted by feeding the observed final-state objects into an algorithm which reconstructs the $t\bar{t}$ dileptonic system kinematics [42, 43] and calculates a measure for the quality of the reconstruction. In addition, the most sensitive spin correlation variables are accessed by reconstructing the four-vectors of the top quark and antiquark in the

event. The algorithm estimates the kinematics of the top quarks for a given jet-lepton combination by obtaining an analytic solution for the system while imposing the following constraints: the $p_{\mathrm{T}}^{\mathrm{miss}}$is assumed to come solely from the two neutrinos, the reconstructed W boson masses must each be equal 80.4 GeV and the mass of the reconstructed top quark and antiquark must be 172.5 GeV. Detector resolution effects are taken into account by smearing both the measured energy and the direction of the leptons and b-jet candidates within their respective resolutions. At each smearing, the solution which gives the smallest invariant mass of the $\mathrm{t\bar{t}}$ system ($\mathrm{m_{t\bar{t}}}$) is chosen (see [44]) and a weight is calculated based on the invariant mass spectrum of the lepton and b-jet from the top quark decay as follows. For each one of the two reconstructed pairs of lepton and b-jet (or assumed b-jet if not tagged), the invariant mass, $m_{\ell b}$, is computed. This is assigned a probability according to the simulated $m_{\ell b}$ coming from a top quark, taken as a probability density function. The event weight is the product of both probabilities. 100 smearings are performed per event and the weights of each smearing are summed over so that the kinematics of the top quark and antiquark are obtained as the weighted average. The lepton-jet combination which gives the maximum sum of weights is chosen. When the event contains two b-tagged jets, the kinematic reconstruction is first performed on the permutation which contains both b-tagged jets. Only in the case when the reconstruction does not yield a solution, are permutations with one or no b-tagged jets considered.

This $\mathrm{t\bar{t}}$ reconstruction process is frequently unable to find solutions for signal-like events since the $p_{\mathrm{T}}^{\mathrm{miss}}$constraint has an additional contribution from the invisible mediator. In the ANN discriminant strategy, a procedure is applied on events failing $\mathrm{t\bar{t}}$ reconstruction that estimates the $p_{\mathrm{T}}^{\mathrm{miss}}$that would be consistent with $\mathrm{t\bar{t}}$ production. The constraint that $p_{\mathrm{T}}^{\mathrm{miss}}$comes solely from two neutrinos is relaxed. This algorithm begins with the original $p_{\mathrm{T}}^{\mathrm{miss}}$and applies a gradient descent method to minimize a cost function which is based on the distance between the $\mathrm{t\bar{t}}$ solution polynomial and the real axis. In every iteration the $p_{\mathrm{T}}^{\mathrm{miss}}$is updated until a solution to the $\mathrm{t\bar{t}}$ system is found. The difference between this amount of $p_{\mathrm{T}}^{\mathrm{miss}}$and the original $p_{\mathrm{T}}^{\mathrm{miss}}$in the event is an estimator of the transverse momentum of the mediator and is denoted as "dark p_T"($p_{\mathrm{T}}^{\mathrm{Dark}}$). This procedure is applied using only the b-tagged jets for events where the b-jet multiplicity is greater than or equal to two, or using all the possible combinations between the b-tagged jet and the other jets otherwise. The full definition of $p_{\mathrm{T}}^{\mathrm{Dark}}$ is as follows. For events where the standard $\mathrm{t\bar{t}}$ reconstruction does not succeed, the variable has positive values, corresponding to the estimation of the mediator p_{T} as explained above. For events where the standard reconstruction does succeed, the variable is defined to be a negative constant with the appropriate dimension (-1000 GeV) multiplied by the weight obtained from the reconstruction. Events where neither of the procedures succeed are discarded. This definition preserves the consistency of the variable in such a way that events with very negative values of $p_{\mathrm{T}}^{\mathrm{Dark}}$ are very compatible with a $\mathrm{t\bar{t}}$ topology, while events with very positive values of $p_{\mathrm{T}}^{\mathrm{Dark}}$ are typically incompatible with a $\mathrm{t\bar{t}}$ topology since the observed amount of $p_{\mathrm{T}}^{\mathrm{miss}}$is not compatible with the neutrino momenta.

6 Analysis strategy

This section outlines the details of the three distinct analysis strategies. All three strategies proceed with a template fit to a preferred discriminating distribution to extract the signal strength of the dark matter signal. The maximum likelihood fits are performed with the Combine tool that uses the ROOSTATS statistical software package [45]. The effects of uncertainties on the normalizations and shapes of signal and background templates are represented as nuisance parameters in the fit. Uncertainties that affect normalization only are modeled using nuisances with log-normal probability densities (lnN). Uncertainties that affect shape, which may also in-

clude an overall normalization effect, are incorporated using a template "morphing" technique. These treatments, as well as the approach used to account for MC statistical uncertainties on template predictions, follow the procedures described in [46]. A full discussion of the systematic uncertainties evaluated is given in Sec. 8. In this section all distributions are shown without systematic uncertainties and without applying the fitted values for the nuisance parameters (pre-fit).

6.1 $p_{\mathrm{T}}^{\mathrm{miss}}$ shape analysis

A potential DM signal could be revealed as an excess of events relative to SM expectations in a region of high $p_{\mathrm{T}}^{\mathrm{miss}}$. The shape of the observed $p_{\mathrm{T}}^{\mathrm{miss}}$ distribution is fitted for the signal extraction procedure. Signal and background $p_{\mathrm{T}}^{\mathrm{miss}}$ templates are derived from simulation and are parameterized to allow for constrained shape and normalization variations in the fits. Events are separated into different flavor ($e\mu$) events and same flavor (ee and $\mu\mu$) events, and further categorized according to the stransverse mass variable, $M_{\mathrm{T2}}^{\ell\ell}$ [47–49]. This variable is defined as

$$M_{\mathrm{T2}}^{\ell\ell} = \min_{\vec{p}_{\mathrm{T1}}^{\mathrm{miss}}+\vec{p}_{\mathrm{T2}}^{\mathrm{miss}}=\vec{p}_{\mathrm{T}}^{\mathrm{miss}}} \left(\max \left[M_{\mathrm{T}} \left(\vec{p}_{\mathrm{T}}^{\,\ell_1}, \vec{p}_{\mathrm{T1}}^{\mathrm{miss}} \right), M_{\mathrm{T}} \left(\vec{p}_{\mathrm{T}}^{\,\ell_2}, \vec{p}_{\mathrm{T2}}^{\mathrm{miss}} \right) \right] \right), \tag{1}$$

where the minimization happens over all possible two-way partitions of $p_{\mathrm{T}}^{\mathrm{miss}}$ in the event. The $M_{\mathrm{T2}}^{\ell\ell}$ distribution has a kinematic endpoint at the W boson mass for dileptonic SM $\mathrm{t\bar{t}}$ events, while the additional contribution to $p_{\mathrm{T}}^{\mathrm{miss}}$ from the DM particles means the distribution for signal has no endpoint. Categories of high signal purity ($M_{\mathrm{T2}}^{\ell\ell} > 110$ GeV) and low purity ($M_{\mathrm{T2}}^{\ell\ell} < 110$ GeV) are defined, giving a total of four regions that are fit simultaneously. Events which have $p_{\mathrm{T}}^{\mathrm{miss}} > 160$ GeV, 3 or more jets, 1 or more b-tagged jets, and both leptons with a p_{T} threshold above 30 GeV are removed from the low purity category, in order to facilitate a combination with a compatible semileptonic $\mathrm{t\bar{t}}$+DM search as has been achieved previously [50]. The low purity category allows the large data yield to provide constraints on uncertainties common to both categories, thereby improving the accuracy of the simulation-based background estimation in the high purity category. The $M_{\mathrm{T2}}^{\ell\ell}$ distribution after event selection for the $p_{\mathrm{T}}^{\mathrm{miss}}$-shape analysis is shown in Fig. 2.

The $p_{\mathrm{T}}^{\mathrm{miss}}$ distributions after selection and categorization are shown in Fig. 3.

6.2 BDT discriminant analysis

The second analysis strategy aims at an improved sensitivity to scenarios with low dark matter mediator masses showing a modest increase in missing transverse energy. Exploring the spin correlation properties of the $\mathrm{t\bar{t}}$ pair gives access to the nature of the DM mediator and can offer additional sensitivity. An interaction with a scalar mediator is expected to give SM-like $\mathrm{t\bar{t}}$ spin correlations while an interaction with a pseudoscalar mediator is expected to yield significant deviations. Kinematic variables based on the amount of $p_{\mathrm{T}}^{\mathrm{miss}}$in the event are combined with spin-sensitive variables in an MVA method to increase the separation between the dark matter signal and the dominant SM $\mathrm{t\bar{t}}$ background. A BDT method using GradientBoost is implemented using the TMVA package [51]. The distribution of the BDT discriminant value is used to set limits on and fit the signal strength. In this analysis, the $p_{\mathrm{T}}^{\mathrm{miss}}$selection is not applied on the $e\mu$ decay channel, and the trailing lepton p_{T} threshold is raised to 20 GeV from 15 GeV.

The following variables were included in the BDT training:

- $p_{\mathrm{T}}^{\mathrm{miss}}$and $p_{\mathrm{T}}^{\mathrm{miss}}$significance: In the $\mathrm{t\bar{t}}$ + DM process there are more invisible particles in the final state than in the $\mathrm{t\bar{t}}$ background, and larger values of $p_{\mathrm{T}}^{\mathrm{miss}}$or

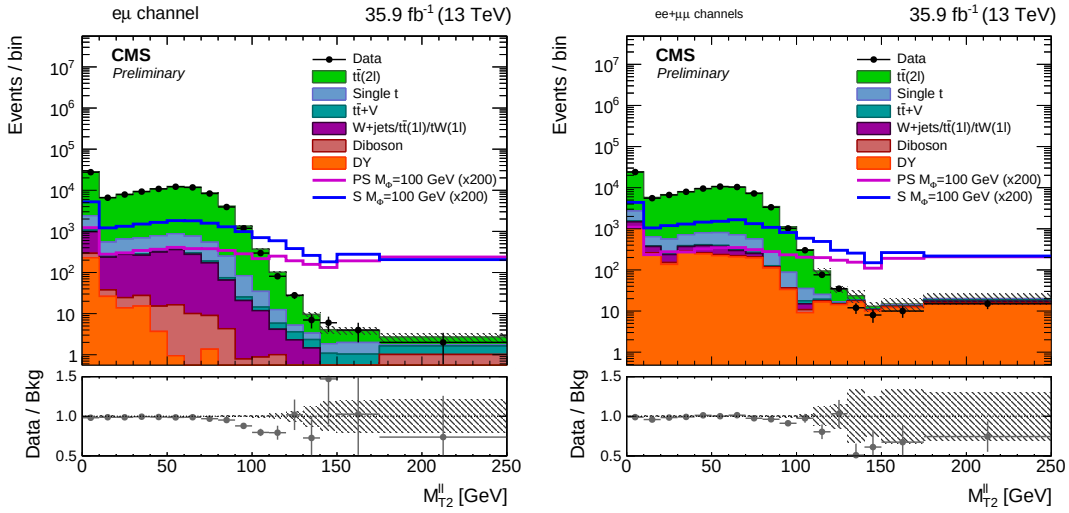

(a) $e\mu$ channel (b) $ee + \mu\mu$ channels

Figure 2: The $M_{\mathrm{T2}}^{\ell\ell}$ distributions for events passing selection requirements for the (a) $e\mu$ and (b) $ee + \mu\mu$ channels. The $M_{\mathrm{T2}}^{\ell\ell}$ distribution of two example signals (scalar and pseudoscalar mediator, $m_{\phi/a} = 100$ GeV) with $m_\chi = 1$ GeV is scaled up by a factor of 200. The last bin includes overflow. Uncertainties are statistical only.

$p_{\mathrm{T}}^{\mathrm{miss}}$significance are therefore to be expected. The $p_{\mathrm{T}}^{\mathrm{miss}}$significance is defined in [52] and is determined from the p-value corresponding to the hypothesis that the observed $p_{\mathrm{T}}^{\mathrm{miss}}$is consistent with a truly zero $p_{\mathrm{T}}^{\mathrm{miss}}$. To calculate the $p_{\mathrm{T}}^{\mathrm{miss}}$significance, the resolution of all observed particles is taken into account.

- $M_{\mathrm{T2}}^{\ell\ell}$: stransverse mass of the dilepton pair as described in Sec. 6.1.
- $M_{\mathrm{T2}}^{\ell b,\ell b}$: stransverse mass of ℓb pairs. This variable is constructed similarly to the $M_{\mathrm{T2}}^{\ell\ell}$ variable but now the lepton is paired up with a b-jet. The ℓb permutation which gives rise to the minimum $M_{\mathrm{T2}}^{\ell b,\ell b}$ is chosen in the event.
- $|\Delta\phi(p_{\mathrm{T}}^{\mathrm{miss}}, \ell\ell)|$: the difference in azimuthal angle between the $p_{\mathrm{T}}^{\mathrm{miss}}$and the dilepton pair in the event.
- kinematic reconstruction weight $\ln(w)$: the weight, w, returned by the kinematic reconstruction algorithm as described in Sec. 5 is a measure for the quality of the $\mathrm{t\bar{t}}$ reconstruction. As the $p_{\mathrm{T}}^{\mathrm{miss}}$in $\mathrm{t\bar{t}}$ + DM events is not solely due to the $\mathrm{t\bar{t}}$ neutrinos, a lower weight is expected in signal events.
- $|\Delta\eta(\ell\ell)|$: the pseudo-rapidity difference between the two leptons in the lab frame.
- $\cos\Phi_{\ell\ell}$: the cosine of the full opening angle between the two leptons in their respective parent rest frames.

The distributions of these variables are shown in Fig. 2 and Figs. 4-6. To ensure sufficient statistics in each bin of the template fit, trainings were chosen which smear the $\mathrm{t\bar{t}}$ background over a large amount of bins. The BDT training at the working point $m_\chi = 1\,\mathrm{GeV}, m_\Phi = 500\,\mathrm{GeV}$ for scalar and pseudoscalar provides generally optimal limits for all mass points of the respective spin hypothesis. The scalar and pseudoscalar hypothesis are trained independently, giving two BDT trainings which are used to evaluate the SM backgrounds and the DM signals to obtain input templates for the fits to data. Below, the BDT discriminant distributions are shown in

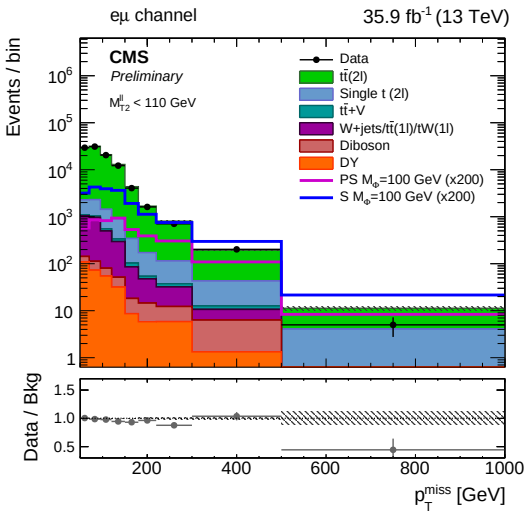

(a) low purity, $e\mu$ channel

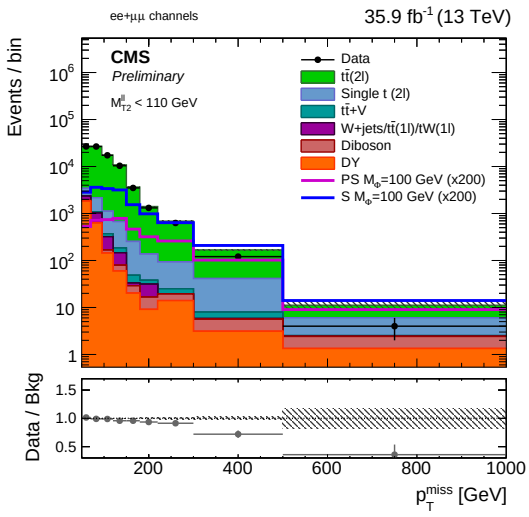

(b) low purity, $ee + \mu\mu$ channels

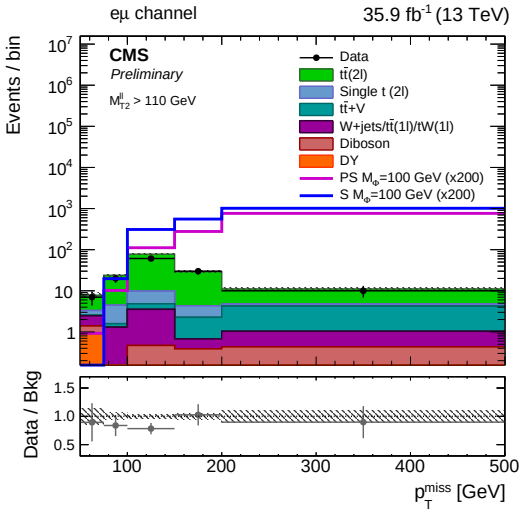

(c) high purity, $e\mu$ channel

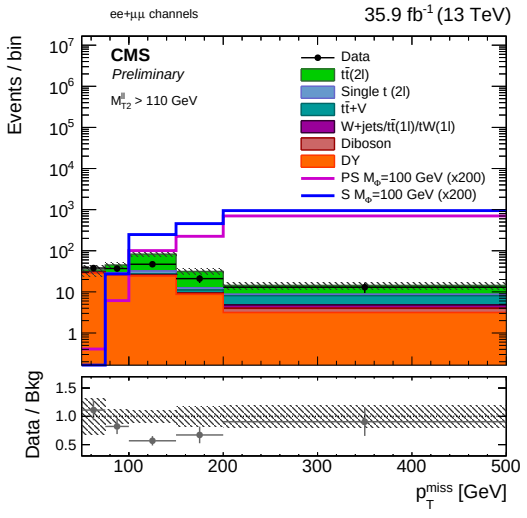

(d) high purity, $ee + \mu\mu$ channels

Figure 3: The pre-fit $p_{\mathrm{T}}^{\mathrm{miss}}$ distributions in the four signal extraction regions. The $p_{\mathrm{T}}^{\mathrm{miss}}$ distribution of two example signals (scalar and pseudoscalar mediator, $m_{\phi/a} = 100$ GeV) with $m_{\chi} = 1$ GeV is scaled up by a factor of 200. The last bin includes overflow. Uncertainties are statistical only.

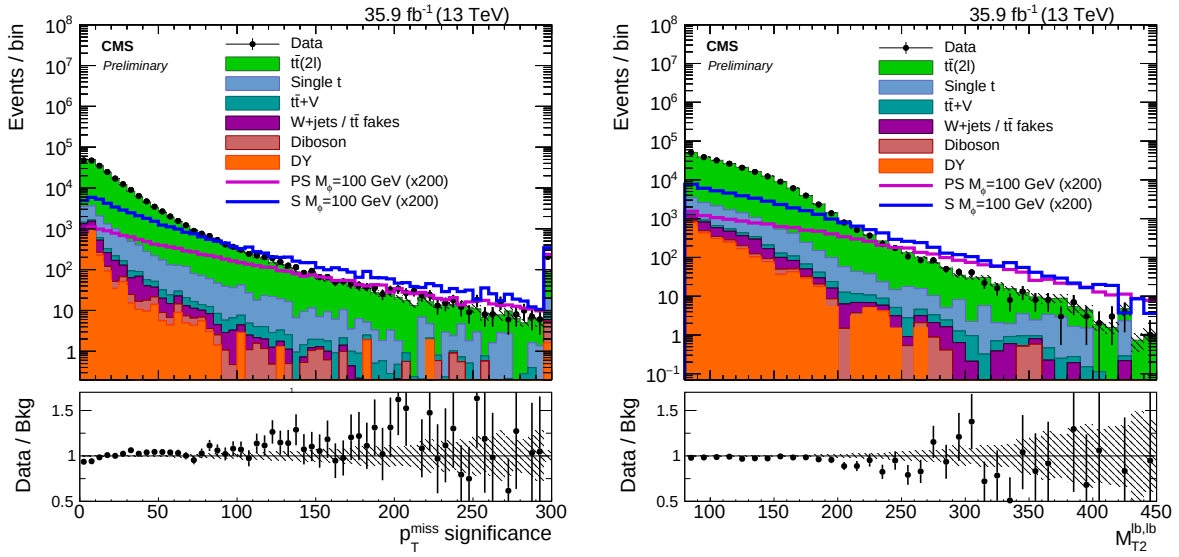

(a) $p_{\mathrm{T}}^{\mathrm{miss}}$ significance (b) $M_{\mathrm{T2}}^{\ell b,\ell b}$

Figure 4: The (a) $p_{\mathrm{T}}^{\mathrm{miss}}$significance and (b) $M_{\mathrm{T2}}^{\ell b,\ell b}$ distributions for events passing selection requirements. The distributions of two example signals (scalar and pseudoscalar mediator, $m_{\phi/a} = 100$ GeV) with $m_{\chi} = 1$ GeV are scaled up by a factor of 200. The ee, $e\mu$ and $\mu\mu$ channels have been combined. The last bin contains overflow. Uncertainties are statistical only.

Fig. 7 for 35.9 fb^{-1} of data for the two background templates with an example signal template superimposed.

6.3 ANN discriminant analysis

The third analysis strategy exploits the discrimination power of the $p_{\mathrm{T}}^{\mathrm{Dark}}$ variable in order to increase the final sensitivity. The $p_{\mathrm{T}}^{\mathrm{Dark}}$ distribution is shown in Fig. 8 for background events and one signal model. To maximize the separation power between DM signals and the top-quark-pair production process, an ANN has been implemented combining $p_{\mathrm{T}}^{\mathrm{Dark}}$ with other variables that have shown discrimination power, such as the $p_{\mathrm{T}}^{\mathrm{miss}}$,$M_{\mathrm{T2}}^{\ell\ell}$, and $\Delta\phi(p_{\mathrm{T}}^{\mathrm{miss}}, \ell\ell)$ variables defined in Sec. 6.2.

Events passing the dilepton selection are used to train an ANN. The ANN strategy, similarly to the BDT, does not apply the $p_{\mathrm{T}}^{\mathrm{miss}}$selection on the $e\mu$ decay channel, and the trailing lepton p_T is raised to 20 GeV from 15 GeV. Figure 8 shows the $p_{\mathrm{T}}^{\mathrm{Dark}}$ distribution used by the ANN as input after this selection. A different ANN training is performed for every signal considered. Fig. 9 shows the shape of the ANN output distribution for background processes and for two different signal models.

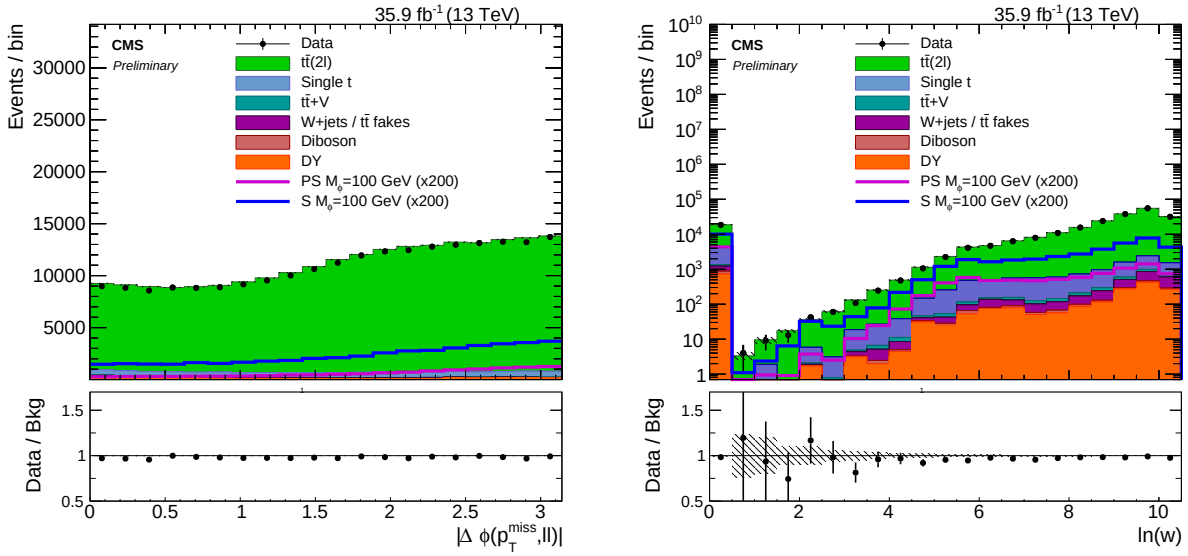

(a) $|\Delta\phi(p_{\mathrm{T}}^{\mathrm{miss}}, \ell\ell)|$ (b) log of kinematic reconstruction weight $\ln w$

Figure 5: The (a) $\Delta\phi(p_{\mathrm{T}}^{\mathrm{miss}}, \ell\ell)$ and the (b) log of the kinematic reconstruction weight ($\ln w$) distributions for events passing selection requirements. The distributions of two example signals (scalar and pseudoscalar mediator, $m_{\phi/a} = 100$ GeV) with $m_\chi = 1$ GeV are scaled up by a factor of 200. The ee, $e\mu$ and $\mu\mu$ channels have been combined. Uncertainties are statistical only.

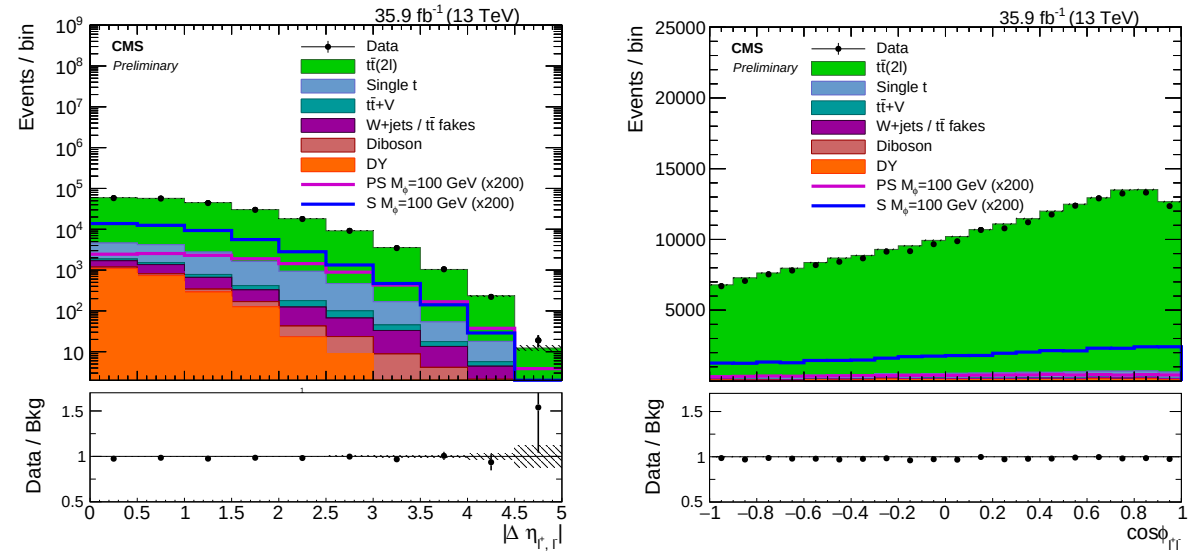

(a) $|\Delta\eta(\ell\ell)|$ (b) $\cos\Phi_{\ell\ell}$

Figure 6: The (a) $\Delta\eta_{\ell^+,\ell^-}$ and (b) $\cos\Phi_{\ell^+\ell^-}$ distributions for events passing selection requirements. The distributions of two example signals (scalar and pseudoscalar mediator, $m_{\phi/a} = 100$ GeV) with $m_\chi = 1$ GeV are scaled up by a factor of 200. The ee, $e\mu$ and $\mu\mu$ channels have been combined. The last bin contains overflow. Uncertainties are statistical only.

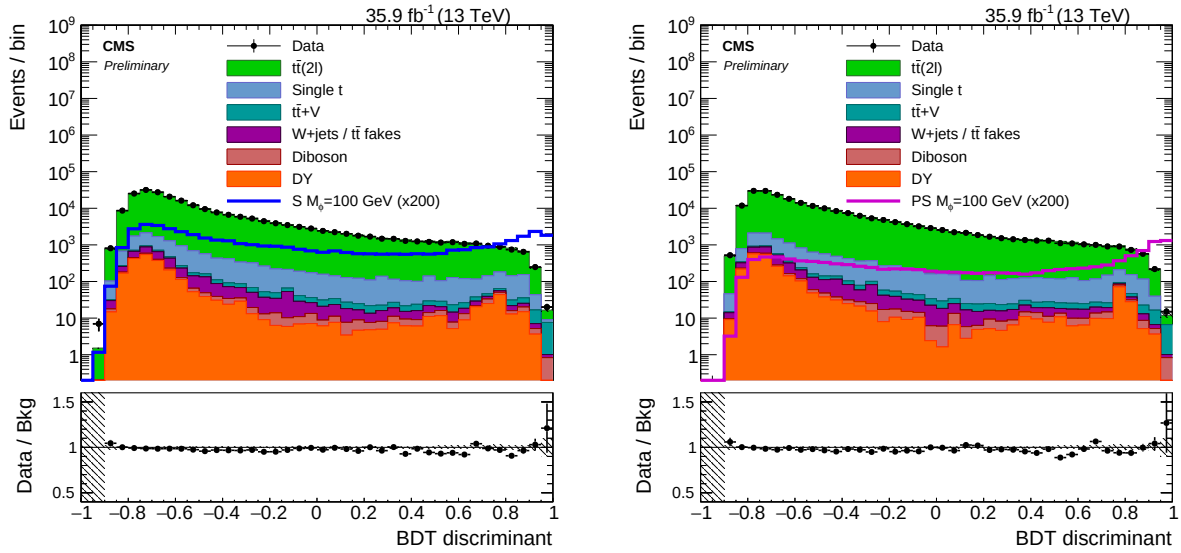

(a) scalar training (b) pseudoscalar training

Figure 7: The pre-fit BDT discriminant distribution trained on the working point 1 GeV dark matter mass and 500 GeV mediator mass for a (a) scalar mediator and a (b) pseudoscalar mediator. The distributions of two example signals (scalar and pseudoscalar mediator, $m_{\phi/a} = 100$ GeV) with $m_\chi = 1$ GeV are scaled up by a factor of 200. The ee, $e\mu$ and $\mu\mu$ channels have been combined. Uncertainties are statistical only.

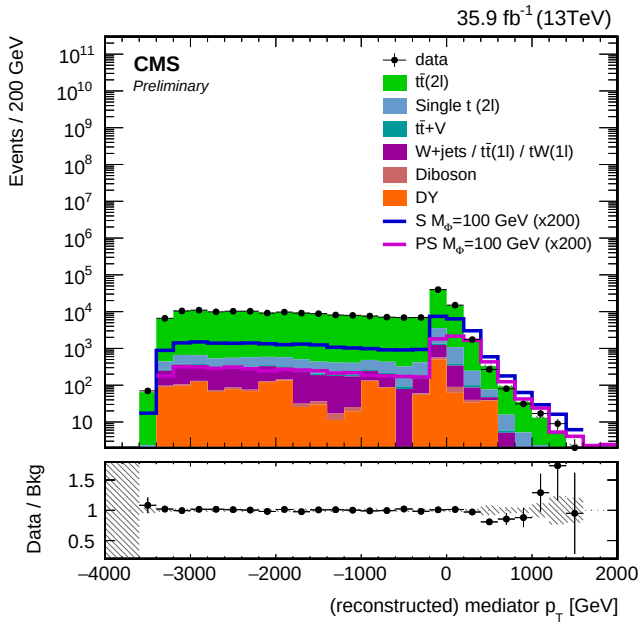

Figure 8: Distribution of the $p_{\mathrm{T}}^{\mathrm{Dark}}$ input variable used to train the ANN for a scalar signal model hypothesis with $m_\chi = 1$ GeV, and $m_\phi = 100$ GeV. The signal distributions are scaled up by a factor of 200. The last bin contains overflow. Uncertainties are statistical only.

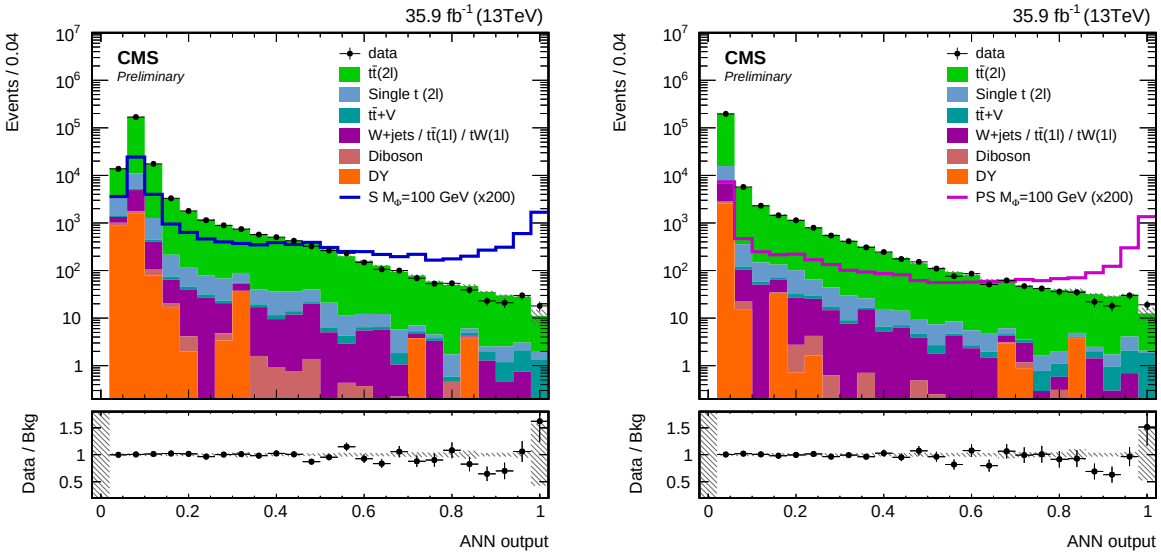

(a) scalar training

(b) pseudoscalar training

Figure 9: Distribution of the ANN discriminant for a signal model with $m_\chi = 1$ GeV and $m_\phi = 100$ for a (a) scalar hypothesis and a (b) pseudoscalar hypothesis. The signal distributions are scaled up by a factor of 200. Uncertainties are statistical only.

7 Background estimation

Many of the background contributions are estimated from simulation. Corrections that aim to reproduce the energy resolution and selection efficiencies as measured in data are applied to the simulations. Furthermore, theoretical and experimental effects that impact the key analysis observables shapes or normalizations are accounted for in the signal extraction procedure. Systematic uncertainties are discussed in Sec. 8.

Data-driven techniques are used to model the DY+Jets background contribution at high $p_{\mathrm{T}}^{\mathrm{miss}}$, since most of this contribution originates from resolution effects that may not be well-modelled by the simulation. The three approaches use the ratio method described below to estimate the normalization of the Drell-Yan background contribution. For the non-prompt lepton background such as events with jets misidentified as leptons, the $p_{\mathrm{T}}^{\mathrm{miss}}$and ANN discriminant approaches estimate the contribution from a data control region, while the BDT discriminant approach uses simulation.

7.1 Drell-Yan background

While simulation is used to estimate the shape of the Drell-Yan process in the designated signal region of each approach, data event yields within 15 GeV of M_Z are used to normalize the Drell-Yan process. The ratio (R) of yields within 15 GeV of M_Z to yields outside this mass window constitute the data to MC normalization scale factors. The predicted Drell-Yan normalization, N_{DY}, is extrapolated from the observed Drell-Yan yield inside the Z boson mass window, N_{in}, according to,

$$N_{\mathrm{DY}} = N_{\mathrm{in}} \frac{R_{\mathrm{MC}}^{0b}}{R_{\mathrm{MC}}^{1b} \cdot R_{\mathrm{Data}}^{0b}} \tag{2}$$

The quantity denoted as R_{MC}^{1b} is the ratio computed in Drell-Yan simulation with all other analysis requirements applied. To account for potential mismodeling of the data mass shape by the simulation, additional ratios are computed in data and simulation with a zero b-tag requirement, denoted R_{Data}^{0b} and R_{MC}^{0b}, respectively.

Non-Drell-Yan processes, namely dileptonic $\mathrm{t\bar{t}}$, are subtracted in the computation of N_{in} and R_{Data}^{0b}. $\mathrm{t\bar{t}}$ to $e\mu$ decays are used to predict the ee or $\mu\mu$ contribution after adjusting for reconstruction and identification efficiency differences between electrons and muons, given the assumption that the branching ratios to electrons and muons is equal. The uncertainty on the Drell-Yan normalization is dominated by the statistical uncertainty on N_{in} and R_{MC}^{1b}.

7.2 Non-prompt lepton background

A jet from processes which only have one prompt electron or muon may be misidentified as an additional "fake" lepton in the final state. Processes falling under this category are semileptonic $\mathrm{t\bar{t}}$, W+jets, and semileptonic tW. The non-prompt lepton rate is measured as the fraction of electron and muon objects passing a less stringent set of isolation and identification requirements, which also pass the tight lepton criteria of the analysis signal region. These objects are referred to as fake-able objects (FO). The fraction, or *fake rate* (FR), is measured in a multi-jet QCD-enriched control region and parametrized in FO p_{T} and η. The measurement is performed in a control region defined by exactly one FO, at least one jet, the azimuthal separation between the FO and leading jet, $\Delta\phi(FO, j_1)$ must be greater than 2, $p_{\mathrm{T}}^{\mathrm{miss}} < 40$ GeV, and transverse mass

computed from the FO transverse momentum and the $p_{\mathrm{T}}^{\mathrm{miss}}$,

$$m_{\mathrm{T}} = \sqrt{2p_{\mathrm{T}}^{\mathrm{FO}} p_{\mathrm{T}}^{\mathrm{miss}}(1 - \cos\Delta\phi_{\mathrm{FO},p_{\mathrm{T}}^{\mathrm{miss}}})}, \tag{3}$$

be less than 35 GeV.

The fake rate is then applied to a single lepton control sample, defined by events with one lepton passing tight isolation and identification requirements, and at least one FO that fails the tight lepton criteria, but passes all other event selection requirements. The non-prompt background normalization is calculated as a sum of the weights of $\mathrm{FR}/(1-\mathrm{FR})$ obtained from each combination of tight-plus-FO pair per event. In other words, the amount of non-prompt leptons entering the signal region is deduced from the FR and the FO failing selection. A significant fraction of this control sample contains true dileptonic events, mainly dileptonic $\mathrm{t\bar{t}}$, and a simulation-based subtraction is performed to avoid an overestimation of the non-prompt lepton background. Any systematic bias of the method is estimated by comparing observation and prediction in a control region of same charge dilepton events, where the non-prompt lepton background is enriched. The uncertainty on the non-prompt lepton background estimate is dominated by the statistical uncertainty of the single lepton control sample.

8 Sources of systematic uncertainty

The following sources of systematic uncertainty, of which the foremost listed are the dominant sources, are accounted for.

- **Jet energy scale (JES).** Reconstructed jet four-momenta in the simulation are simultaneously varied according to the uncertainty on jet energy scale. Jet energy scale uncertainties are coherently propagated to all observables including $p_{\mathrm{T}}^{\mathrm{miss}}$, $p_{\mathrm{T}}^{\mathrm{miss}}$significance, $M_{\mathrm{T2}}^{\ell\ell}$, and $M_{\mathrm{T2}}^{\ell b,\ell b}$. Uncertainty effects due to the jet energy resolution were found to be negligible.
- **Factorization and renormalization scales.** Uncertainties due to the renormalization scale μ_R and the factorization scale μ_F in the simulation matrix-element generator are modeled by varying the scales independently by a factor of 0.5 or 2, and propagating the changes to the distributions used in the fit. This is accommodated via weights obtained directly from the generator information in the MC simulation where available. The uncertainty is considered to be uncorrelated among the different background processes.
- **Fake $p_{\mathrm{T}}^{\mathrm{miss}}$uncertainty.** For the $M_{\mathrm{T2}}^{\ell\ell} > 110\,\mathrm{GeV}$ category, an uncertainty is assigned to MC derived background shapes to account for potential mismodeling of the rate of events with large fake $p_{\mathrm{T}}^{\mathrm{miss}}$ in simulation. This uncertainty is derived as a function of hadronic recoil using $Z(\ell\ell)$ events passing $M_{\mathrm{T2}}^{\ell\ell} > 110\,\mathrm{GeV}$. This uncertainty is only applied in the $p_{\mathrm{T}}^{\mathrm{miss}}$ strategy as a variation of the unclustered energy uncertainty.
- **Unclustered energy.** The variation of the unclustered energy is propagated to the $p_{\mathrm{T}}^{\mathrm{miss}}$in the event, and the BDT and ANN discriminant approaches evaluate this uncertainty on all processes.
- **PDF uncertainties.** Uncertainties on the parton distribution functions are estimated by re-weighting the samples with the NNPDF3.0 [17] replicas [53].
- **Single top and diboson normalization.** The expected yields for background processes are either scaled to data or to theory predictions with the best available accu-

racy. The uncertainties on the cross section predictions are taken into account in the PDF as well as renormalization and factorization scale uncertainties. In the single top and diboson simulation samples, these variations are not available, so an uncertainty of 20% and 10% is assigned respectively to the normalizations and these uncertainties are treated independently of each other.

- **Pileup modeling.** Systematic uncertainties due to pileup modeling are taken into account by varying the minimum bias cross section of 69 mb used to calculate the data pileup distributions by $\pm 4.6\%$.
- **Luminosity.** An uncertainty of 2.5% is taken on the integrated luminosity of the data sample [54].
- **Lepton reconstruction and selection.** The uncertainty on lepton reconstruction and selection efficiency is associated with the efficiency measurement with samples of Z bosons decaying to dielectrons or dimuons. The p_{T}- and η-dependent scale factors are varied within their uncertainties which amounts to $\approx 2\%$ per lepton.
- **Lepton trigger.** The uncertainty on lepton triggering efficiency is associated with the efficiency measurement with samples of Z bosons decaying to dielectrons or dimuons. The corresponding uncertainty ranges from 1% to 2%.
- **b-tagging efficiency.** The b-tagging efficiency and the respective uncertainty is measured on independent control samples. Uncertainties from gluon splitting, the b quark fragmentation function, the selections used to define the control samples, etc. are propagated to the efficiency scale factors [55].
- **Simulation statistics.** Shape uncertainties due to the limited size of the simulated signal and background samples are included by allowing each bin of the distributions included in the signal extraction to fluctuate independently according to the statistical uncertainty on the simulation.

The following sources of systematic uncertainty are accounted for on the pertinent sub-dominant background processes in the signal regions. The uncertainty associated with the fake lepton background is the sole uncertainty applied to this process, where the rest are applied in addition to the aforementioned sources of systematic uncertainty.

- **Misidentified lepton background.** The sources of uncertainty on the misidentified lepton background stem from the uncertainty on the measured misidentification rate, and from the statistical uncertainty of the single lepton control sample to which the rate is applied. The uncertainties per channel are: 78% (ee), 70% ($e\mu$), 74% ($\mu\mu$) in the high signal purity category and 47% (ee), 12% ($e\mu$), and 20% ($\mu\mu$) in the low signal purity category, and are dominated by the statistical uncertainty of the application sample. This uncertainty is applied as such on the $p_{\mathrm{T}}^{\mathrm{miss}}$analysis strategy. In the ANN analysis this background is estimated using the same technique and a weighted average of the per-channel uncertainties listed earlier is applied, as the signal extraction distribution is not split by lepton flavor. In the BDT analysis strategy, the misidentified lepton background is estimated from the $\mathrm{t\bar{t}}$ simulation and an uncertainty of 50% is associated to it.
- **Drell-Yan background.** The uncertainties on the data-driven Drell-Yan background estimates in the dileptonic channels are 11% (ee) and 6% ($\mu\mu$). This uncertainty is applied as such on the $p_{\mathrm{T}}^{\mathrm{miss}}$ analysis strategy. In the ANN analysis the dependency on $M_{\mathrm{T2}}^{\ell\ell}$ of the Drell–Yan scale factor is studied, and the maximum deviation found, 30%, is assessed as a systematic uncertainty. In the BDT analysis strategy, the uncertainty on the Drell-Yan background covers the dependence of the data-driven Drell-Yan

scaling on the $p_{\mathrm{T}}^{\mathrm{miss}}$content in the event by applying an uncertainty up to 300% at the largest BDT discriminant values.

- **Top p_{T} reweighting.** Differential measurements of top-quark pair production show that measured p_{T} spectrum of top quarks is softer than in simulation. Scale factors to cover this effect are derived in previous CMS measurements and are applied in the analysis by default. An associated systematic uncertainty is estimated by not applying the scale factor re-weighting.

9 Results

Upper limits on the signal cross section have been calculated at 95% confidence level (CL) using the CL_s criterion and an asymptotic formulation [56–59]. This method takes into account the statistical and systematic uncertainties in the signal and background templates for the fitted observable in each strategy ($p_{\mathrm{T}}^{\mathrm{miss}}$, BDT discriminant, ANN discriminant). The templates are split according to same and opposite flavor leptons in the $p_{\mathrm{T}}^{\mathrm{miss}}$shape strategy, whereas the lepton channels are combined in the each of the MVA strategy templates. The background templates are split according to the following processes: $\mathrm{t\bar{t}}$ (2ℓ), fakes (comprising W+jets, $\mathrm{t\bar{t}}$ (1ℓ), and tW(1ℓ)), $\mathrm{t\bar{t}}$ +V, single top, DY+jets, and dibosons. The normalizations and shapes of both the background and signal processes are varied according to the nuisance parameters which are constrained according to the uncertainties listed in Sec. 8. The data has been fit with both the background-only and background-plus-signal hypotheses. The background hypothesis post-fit distributions for the discriminant variable employed by each strategy for a chosen scalar and pseudoscalar working point are shown in Fig. 10−12. No significant excess in any of the respective search strategy channels is observed and limits are set on the signal strength (μ), which is defined as the ratio of the signal cross section to the theoretical cross section, $\mu = \frac{\sigma}{\sigma_{TH}}$. Explicit checks have been performed for a few signal mass samples demonstrating the consistency of the results yielded by the asymptotic approximation with results from the full CL_s calculation. A good fit quality has been ascertained by the fit nuisance parameter pulls produced using Asimov toy experiments and the data. The expected and observed limits on the strength of $\mathrm{t\bar{t}}$+DM production as a function of mediator mass, with unitary couplings to SM fermions and DM particles are shown in Fig. 13 and Tables 2− 3 for the respective strategies.

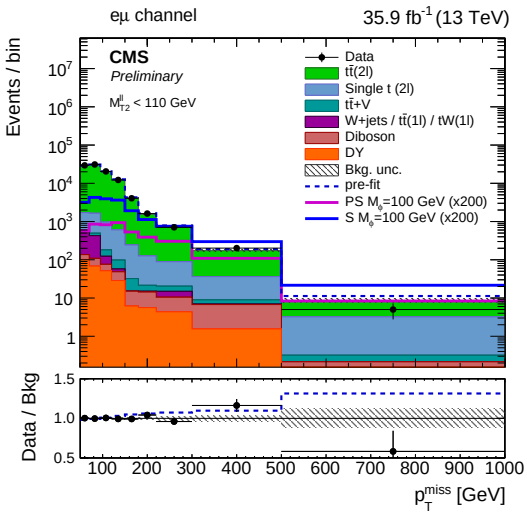

(a) low purity, $e\mu$ channel

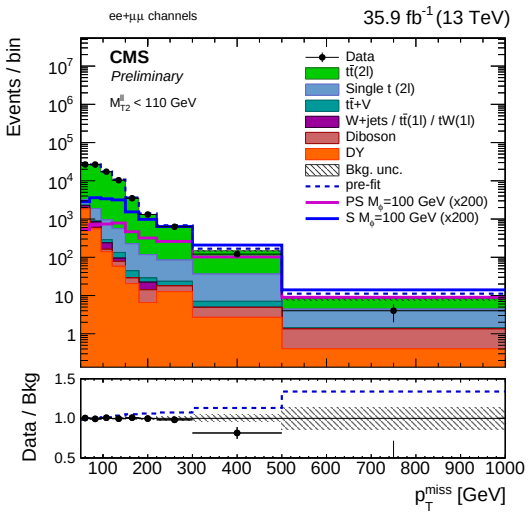

(b) low purity, $ee + \mu\mu$ channels

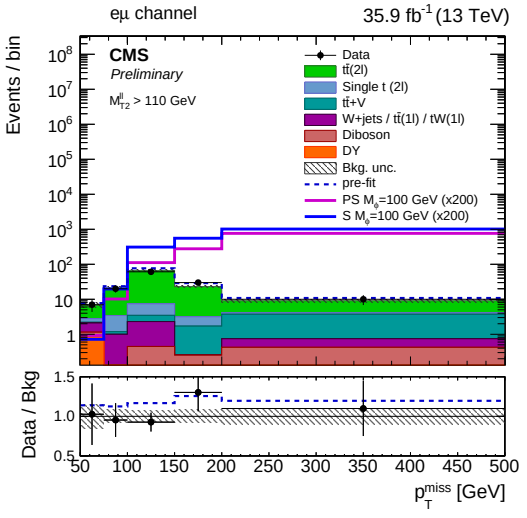

(c) high purity, $e\mu$ channel

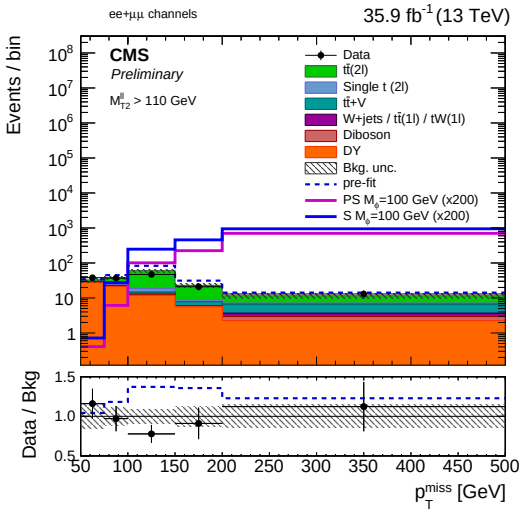

(d) high purity, $ee + \mu\mu$ channels

Figure 10: The post-fit $p_{\mathrm{T}}^{\mathrm{miss}}$ distributions in the four signal extraction regions of the $p_{\mathrm{T}}^{\mathrm{miss}}$ shape analysis. The pre-fit $p_{\mathrm{T}}^{\mathrm{miss}}$ distributions for two example signals (scalar and pseudoscalar mediator, $m_{\phi/a} = 100$ GeV) with $m_{\chi} = 1$ GeV are scaled up by a factor of 200. The last bin includes overflow. Statistical and systematic uncertainties are shown.

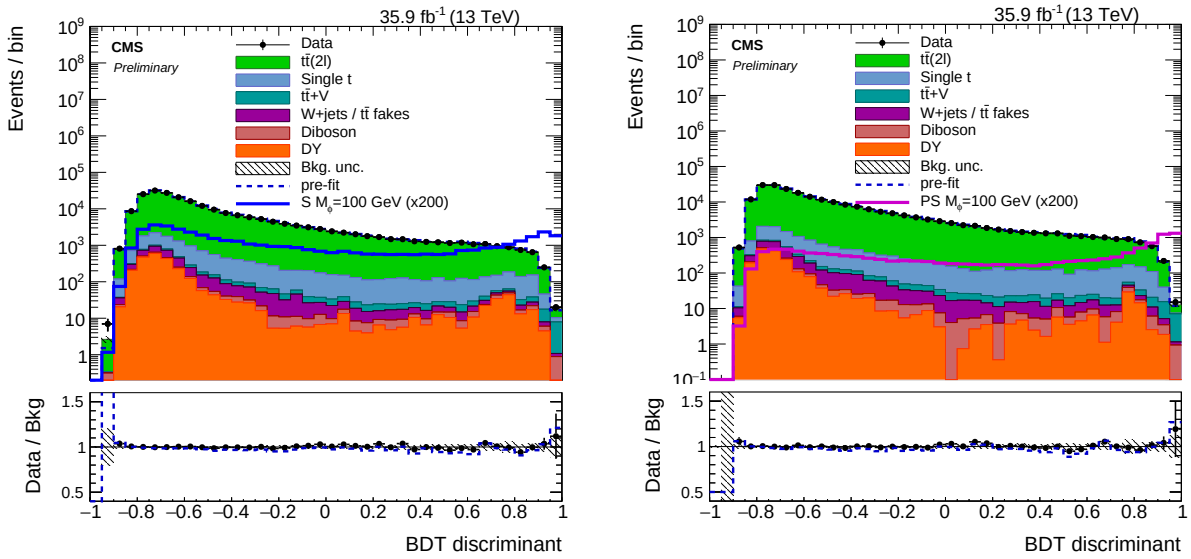

(a) scalar training (b) pseudoscalar training

Figure 11: The post-fit BDT discriminant distribution in the signal region trained on the working point for $m_\phi = 500$ GeV, $m_\chi = 1$ GeV for a (a) scalar mediator and a (b) pseudoscalar mediator. The pre-fit BDT discriminant distributions for two example signals (scalar and pseudoscalar mediator, $m_{\phi/a} = 100$ GeV) with $m_\chi = 1$ GeV are scaled up by a factor of 200. Statistical and systematic uncertainties are shown.

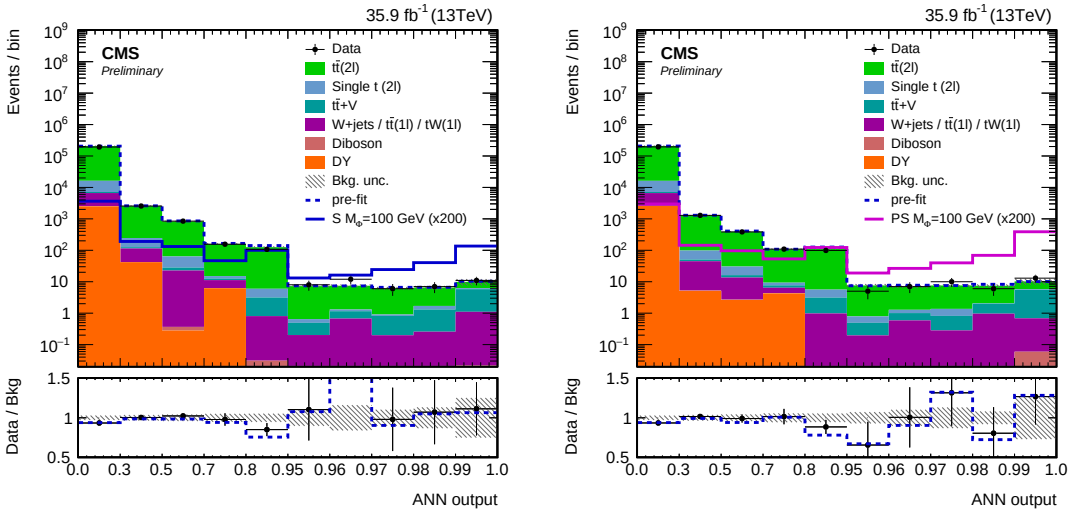

(a) scalar training (b) pseudoscalar training

Figure 12: The post-fit ANN discriminant distribution in the signal region trained on the working point for $m_{\phi/a} = 100$ GeV, $m_\chi = 1$ GeV for a (a) scalar mediator and a (b) pseudoscalar mediator. The pre-fit ANN discriminant distributions for two example signals (scalar and pseudoscalar mediator, $m_{\phi/a} = 100$ GeV) with $m_\chi = 1$ GeV are scaled up by a factor of 200. Statistical and systematic uncertainties are shown. The apparent bin width has been fixed to the same size to improve the clarity. The axis labels indicate the actual sizes of the different bins.

Table 2: Expected and observed limits on the signal strength including the one sigma uncertainties for 35.9 fb^{-1} of data for the scalar hypothesis with $m_\chi = 1$ GeV in the respective strategies.

	p_T^miss		BDT		ANN	
m_ϕ GeV	expected	observed	expected	observed	expected	observed
10	0.59 ± 0.37	0.72	0.48 ± 0.30	0.56	0.51 ± 0.29	0.36
20	0.51 ± 0.33	0.64	0.43 ± 0.28	0.49	0.46 ± 0.27	0.35
50	0.62 ± 0.40	0.74	0.56 ± 0.36	0.69	0.55 ± 0.33	0.64
100	1.01 ± 0.64	1.29	0.91 ± 0.57	1.13	0.93 ± 0.55	0.99
200	2.40 ± 1.48	2.97	2.14 ± 1.32	2.67	2.37 ± 1.36	2.89
300	4.61 ± 3.15	5.64	4.05 ± 2.77	5.05	4.22 ± 2.68	5.47
500	18.7 ± 15.2	22.9	16.3 ± 13.2	20.2	15.8 ± 11.9	20.5

Table 3: Expected and observed limits on the signal strength including the one sigma uncertainties for 35.9 fb^{-1} of data for the pseudoscalar hypothesis with $m_\chi = 1$ GeV in the respective strategies.

	p_T^miss		BDT		ANN	
m_ϕ GeV	expected	observed	expected	observed	expected	observed
10	0.92 ± 0.64	1.16	0.73 ± 0.52	1.04	0.78 ± 0.52	1.01
20	0.92 ± 0.64	1.16	0.72 ± 0.50	1.00	0.77 ± 0.50	0.81
50	1.00 ± 0.72	1.26	0.79 ± 0.56	1.10	0.86 ± 0.56	1.03
100	1.18 ± 0.85	1.49	0.94 ± 0.67	1.32	0.99 ± 0.67	1.19
200	1.95 ± 1.34	2.45	1.54 ± 1.06	2.14	1.77 ± 1.13	2.18
300	3.23 ± 2.48	3.99	2.56 ± 1.97	3.53	2.73 ± 1.98	3.13
500	18.1 ± 14.5	22.3	14.2 ± 11.4	19.6	15.0 ± 11.2	19.9

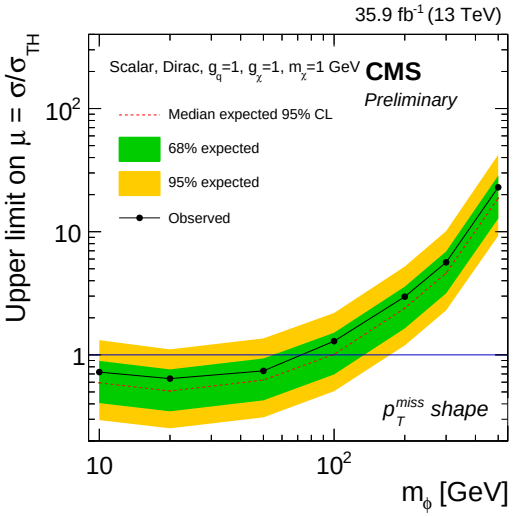

(a) $p_{\mathrm{T}}^{\mathrm{miss}}$ shape: scalar mediator

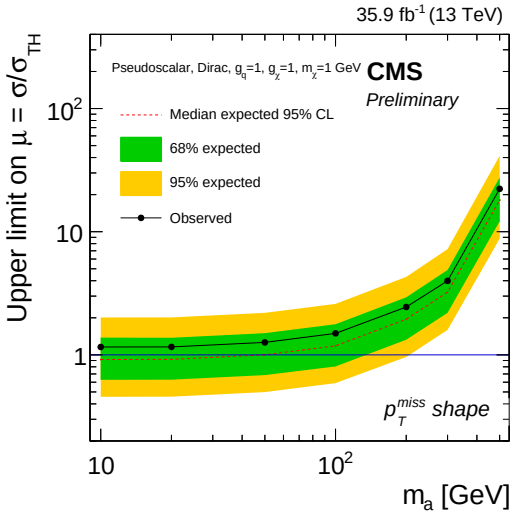

(b) $p_{\mathrm{T}}^{\mathrm{miss}}$ shape: pseudoscalar mediator

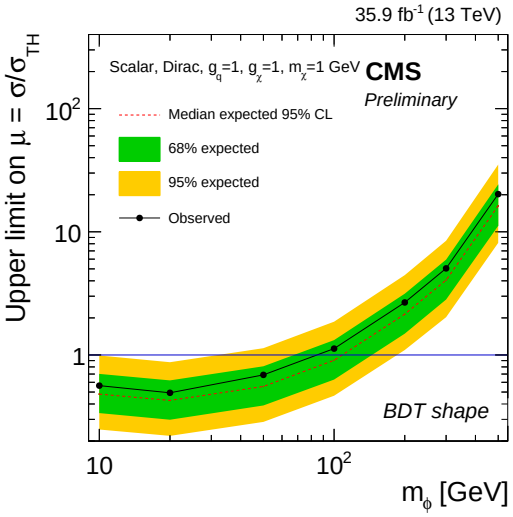

(c) BDT discriminant: scalar mediator

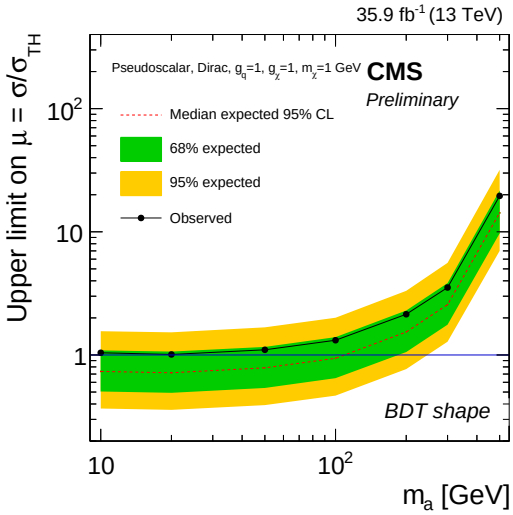

(d) BDT discriminant: pseudoscalar mediator

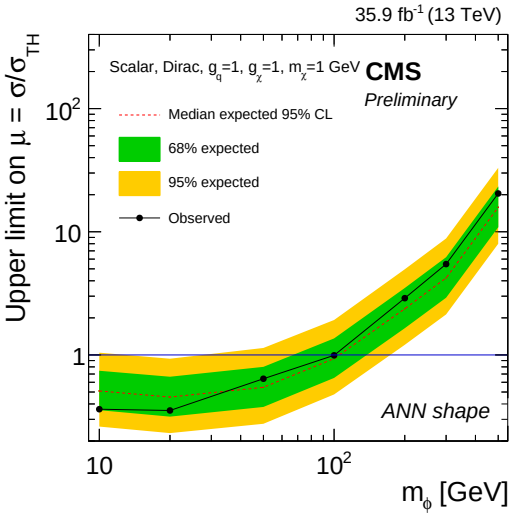

(e) ANN discriminant: scalar mediator

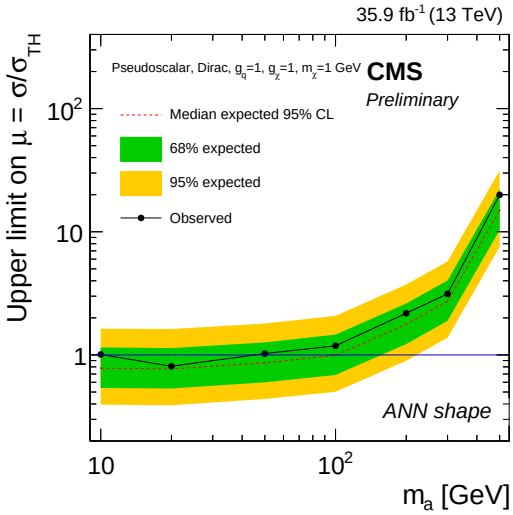

(f) ANN discriminant: pseudoscalar mediator

Figure 13: The expected and observed limits for the three different strategies for scalar (left) and pseudoscalar models (right) with $m_\chi = 1$ GeV and $g_{\mathrm{q}} = g_\chi = 1$.

9.1 Interpretation

The results from the search strategies described exemplify the potential to gain sensitivity by including additional information that helps distinguish the SM dilepton $\mathrm{t\bar{t}}$ process from the $\mathrm{t\bar{t}}$ +DM process. Using such relevant observables as $p_{\mathrm{T}}^{\mathrm{miss}}$, stransverse mass ($M_{\mathrm{T2}}^{\ell\ell}$), $\Delta\phi(p_{\mathrm{T}}^{\mathrm{miss}}, \ell\ell)$, and a derivative of the kinematic reconstruction of the $\mathrm{t\bar{t}}$ system to train a discriminating ANN output yields gains over a $p_{\mathrm{T}}^{\mathrm{miss}}$-$M_{\mathrm{T2}}^{\ell\ell}$ fit strategy as seen in Fig. 14, when comparing the ANN shape (orange) and $p_{\mathrm{T}}^{\mathrm{miss}}$ shape (magenta) expected limit curves. Furthermore, a gain in sensitivity is observed with the addition of information pertaining to the spin nature of the mediator which helps discriminate between scalar (SM-like) and pseudoscalar mediated DM production. The BDT approach uses the spin sensitive variables along with the aforementioned observables in an MVA method to train an output variable which provides the added sensitivity, particularly for the pseudoscalar mediator hypothesis as shown in Fig. 14.

Assuming coupling values of $g_{\mathrm{q}} = g_{\chi} = 1$ and DM mass $m_{\chi} = 1$ GeV, the expected 95% CL exclusions for a scalar mediator are $m_{\phi} < 99$ GeV, $m_{\phi} < 107$ GeV, and $m_{\phi} < 105$ GeV using the $p_{\mathrm{T}}^{\mathrm{miss}}$ shape, BDT discriminant, and ANN discriminant strategies respectively, which highlights the gains from each strategy. The respective observed 95% CL exclusions for a scalar mediator are $m_{\phi} < 74$ GeV, $m_{\phi} < 85$ GeV, and $m_{\phi} < 101$ GeV using the $p_{\mathrm{T}}^{\mathrm{miss}}$ shape, BDT discriminant, and ANN discriminant strategies. Analogously, the expected exclusions achieved for a pseudoscalar mediator are $m_a < 50$ GeV, $m_a < 110$ GeV, and $m_a < 100$ GeV using the $p_{\mathrm{T}}^{\mathrm{miss}}$ shape, BDT discriminant, and ANN discriminant strategies, respectively. The $p_{\mathrm{T}}^{\mathrm{miss}}$ shape strategy does not observe a 95% CL exclusion, while the BDT discriminant observes exclusion at $m_a = 100$ GeV, and the ANN discriminant observes exclusion for $m_a < 46$ GeV, for a pseudoscalar mediator. The observed (expected) upper limits on the cross section for scalar mediators range from 14.6 (12.5) pb to 0.16 (0.13) pb for $m_{\phi} = 10$ GeV to $m_{\phi} = 500$ GeV, respectively. For the same mass range, the observed (expected) upper limits on the cross section for pseudoscalar mediators are 0.65 (0.45) pb to 0.16 (0.12) pb.

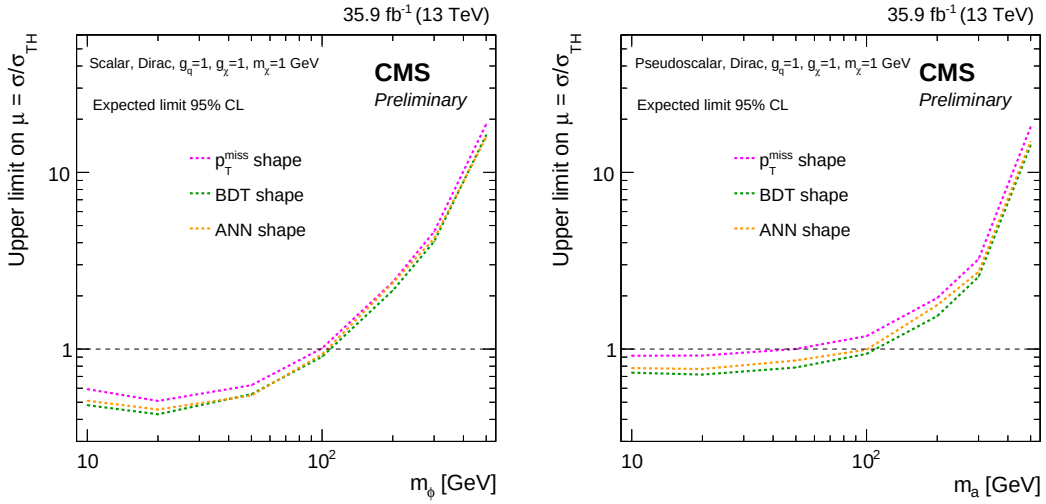

(a) scalar mediator

(b) pseudoscalar mediator

Figure 14: The expected limits at 95% CL for the $p_{\mathrm{T}}^{\mathrm{miss}}$ shape (magenta), BDT shape (green), and ANN shape (orange) strategies for (a) scalar and (b) pseudoscalar models with $m_{\chi} = 1$ GeV and $g_{\mathrm{q}} = g_{\chi} = 1$.

10 Conclusions

A search for an excess of events with large $p_{\mathrm{T}}^{\mathrm{miss}}$ produced in association with a top quark pair decaying to the dilepton final state has been presented. The integrated luminosity of the proton-proton collision data sample used corresponds to 35.9 fb^{-1}, and was collected by the CMS detector at $\sqrt{s} = 13$ TeV at the LHC during 2016. Observations are consistent with no significant deviation from the SM background expectation in the $p_{\mathrm{T}}^{\mathrm{miss}}$ spectrum, the BDT discriminant distribution, and the ANN discriminant distribution in same and opposite lepton flavor channels. Results are interpreted in terms of simplified dark matter (DM) models with scalar and pseudoscalar mediators using the NLO cross sections as shown in Table 1. Assuming coupling values of $g_{\mathrm{q}} = g_{\chi} = 1$ and DM mass $m_{\chi} = 1$ GeV, the observed (expected) 95% CL exclusions for a scalar mediator are $m_{\phi} < 74\,(99)$ GeV, and the expected exclusion for a pseudoscalar mediator is $m_a < 50$ GeV, while no pseudoscalar mediator exclusion is observed using the $p_{\mathrm{T}}^{\mathrm{miss}}$ shape strategy. This result improves upon the previous search for dark matter production in association with a top quark pair [50] performed using a data sample with integrated luminosity of 2.2 fb^{-1} collected by the CMS detector at $\sqrt{s} = 13$ TeV at the LHC during 2015. The previous search fell short of observing and expecting to observe an exclusion at 95% CL for simplified DM models with scalar and pseudoscalar mediators.

Acknowledgments

We congratulate our colleagues in the CERN accelerator departments for the excellent performance of the LHC and thank the technical and administrative staffs at CERN and at other CMS institutes for their contributions to the success of the CMS effort. In addition, we gratefully acknowledge the computing centers and personnel of the Worldwide LHC Computing Grid for delivering so effectively the computing infrastructure essential to our analyses. Finally, we acknowledge the enduring support for the construction and operation of the LHC and the CMS detector provided by the following funding agencies: the Austrian Federal Ministry of Science, Research and Economy and the Austrian Science Fund; the Belgian Fonds de la Recherche Scientifique, and Fonds voor Wetenschappelijk Onderzoek; the Brazilian Funding Agencies (CNPq, CAPES, FAPERJ, and FAPESP); the Bulgarian Ministry of Education and Science; CERN; the Chinese Academy of Sciences, Ministry of Science and Technology, and National Natural Science Foundation of China; the Colombian Funding Agency (COLCIENCIAS); the Croatian Ministry of Science, Education and Sport, and the Croatian Science Foundation; the Research Promotion Foundation, Cyprus; the Ministry of Education and Research, Estonian Research Council via IUT23-4 and IUT23-6 and European Regional Development Fund, Estonia; the Academy of Finland, Finnish Ministry of Education and Culture, and Helsinki Institute of Physics; the Institut National de Physique Nucléaire et de Physique des Particules / CNRS, and Commissariat à l'Énergie Atomique et aux Énergies Alternatives / CEA, France; the Bundesministerium für Bildung und Forschung, Deutsche Forschungsgemeinschaft, and Helmholtz-Gemeinschaft Deutscher Forschungszentren, Germany; the General Secretariat for Research and Technology, Greece; the National Scientific Research Foundation, and National Innovation Office, Hungary; the Department of Atomic Energy and the Department of Science and Technology, India; the Institute for Studies in Theoretical Physics and Mathematics, Iran; the Science Foundation, Ireland; the Istituto Nazionale di Fisica Nucleare, Italy; the Ministry of Science, ICT and Future Planning, and National Research Foundation (NRF), Republic of Korea; the Lithuanian Academy of Sciences; the Ministry of Education, and University of Malaya

(Malaysia); the Mexican Funding Agencies (CINVESTAV, CONACYT, SEP, and UASLP-FAI); the Ministry of Business, Innovation and Employment, New Zealand; the Pakistan Atomic Energy Commission; the Ministry of Science and Higher Education and the National Science Centre, Poland; the Fundação para a Ciência e a Tecnologia, Portugal; JINR, Dubna; the Ministry of Education and Science of the Russian Federation, the Federal Agency of Atomic Energy of the Russian Federation, Russian Academy of Sciences, and the Russian Foundation for Basic Research; the Ministry of Education, Science and Technological Development of Serbia; the Secretaría de Estado de Investigación, Desarrollo e Innovación and Programa Consolider-Ingenio 2010, Spain; the Swiss Funding Agencies (ETH Board, ETH Zurich, PSI, SNF, UniZH, Canton Zurich, and SER); the Ministry of Science and Technology, Taipei; the Thailand Center of Excellence in Physics, the Institute for the Promotion of Teaching Science and Technology of Thailand, Special Task Force for Activating Research and the National Science and Technology Development Agency of Thailand; the Scientific and Technical Research Council of Turkey, and Turkish Atomic Energy Authority; the National Academy of Sciences of Ukraine, and State Fund for Fundamental Researches, Ukraine; the Science and Technology Facilities Council, UK; the US Department of Energy, and the US National Science Foundation.

Individuals have received support from the Marie-Curie program and the European Research Council and EPLANET (European Union); the Leventis Foundation; the A. P. Sloan Foundation; the Alexander von Humboldt Foundation; the Belgian Federal Science Policy Office; the Fonds pour la Formation à la Recherche dans l'Industrie et dans l'Agriculture (FRIA-Belgium); the Agentschap voor Innovatie door Wetenschap en Technologie (IWT-Belgium); the Ministry of Education, Youth and Sports (MEYS) of the Czech Republic; the Council of Science and Industrial Research, India; the HOMING PLUS program of Foundation for Polish Science, cofinanced from European Union, Regional Development Fund; the Compagnia di San Paolo (Torino); the Consorzio per la Fisica (Trieste); MIUR project 20108T4XTM (Italy); the Thalis and Aristeia programs cofinanced by EU-ESF and the Greek NSRF; and the National Priorities Research Program by Qatar National Research Fund.

References

[1] F. Zwicky, "On the Masses of Nebulae and of Clusters of Nebulae", *Astrophys. J.* **86** (October, 1937) 217, doi:10.1086/143864.

[2] M. Persic, P. Salucci, and F. Stel, "The Universal rotation curve of spiral galaxies: 1. The Dark matter connection", *Mon. Not. Roy. Astron. Soc.* **281** (1996) 27, doi:10.1093/mnras/281.1.27,10.1093/mnras/278.1.27, arXiv:astro-ph/9506004.

[3] D. Walsh, R. F. Carswell, and R. J. Weymann, "0957 + 561 A, B - Twin quasistellar objects or gravitational lens", **279** (May, 1979) 381–384, doi:10.1038/279381a0.

[4] G. t'Hooft, "Naturalness, chiral symmetry, and spontaneous chiral symmetral breaking", *NATO Sci. Ser. B* **59** (1980) 135.

[5] E. Witten, "Dynamical breaking of supersymmetry", *Nuclear Physics B* **188** (1981) 513, doi:https://doi.org/10.1016/0550-3213(81)90006-7.

[6] S. Dimopoulos and H. Georgi, "Softly broken supersymmetry and su(5)", *Nuclear Physics B* **193** (1981) 150, doi:https://doi.org/10.1016/0550-3213(81)90522-8.

[7] G. Steigman and M. S. Turner, "Cosmological constraints on the properties of weakly interacting massive particles", *Nuclear Physics B* **253** (1985), no. Supplement C, 375 – 386, doi:https://doi.org/10.1016/0550-3213(85)90537-1.

[8] G. D'Ambrosio, G. Giudice, G. Isidori, and A. Strumia, "Minimal flavour violation: an effective field theory approach", *Nuclear Physics B* **645** (2002), no. 1, 155 – 187, doi:10.1016/S0550-3213(02)00836-2.

[9] G. Isidori and D. M. Straub, "Minimal flavour violation and beyond", *Eur. Phys. J. C* **72** (Aug, 2012) 2103, doi:10.1140/epjc/s10052-012-2103-1.

[10] J. Abdallah et al., "Simplified Models for Dark Matter Searches at the LHC", *Phys. Dark Univ.* **9-10** (2015) 8–23, doi:10.1016/j.dark.2015.08.001, arXiv:1506.03116.

[11] D. Abercrombie et al., "Dark Matter Benchmark Models for Early LHC Run-2 Searches: Report of the ATLAS/CMS Dark Matter Forum", arXiv:1507.00966.

[12] M. Bauer et al., "Towards the next generation of simplified Dark Matter models", arXiv:1607.06680.

[13] J. Alwall et al., "The automated computation of tree-level and next-to-leading order differential cross sections, and their matching to parton shower simulations", *JHEP* **07** (2014) 079, doi:10.1007/JHEP07(2014)079, arXiv:1405.0301.

[14] P. Artoisenet et al., "Automatic spin-entangled decays of heavy resonances in Monte Carlo simulations", *JHEP* **03** (2013) 015, doi:10.1007/JHEP03(2013)015, arXiv:1212.3460.

[15] J. Alwall et al., "Comparative study of various algorithms for the merging of parton showers and matrix elements in hadronic collisions", *Eur. Phys. J.* **C53** (2008) 473–500, doi:10.1140/epjc/s10052-007-0490-5, arXiv:0706.2569.

[16] P. Harris, V. V. Khoze, M. Spannowsky, and C. Williams, "Constraining dark sectors at colliders: Beyond the effective theory approach", *Phys. Rev. D* **91** (2015) 055009, doi:10.1103/PhysRevD.91.055009.

[17] R. D. Ball et al., "Parton distributions for the lhc run ii", *JHEP* **2015** (Apr, 2015) 40, doi:10.1007/JHEP04(2015)040.

[18] T. Sjöstrand, S. Mrenna, and P. Skands, "PYTHIA 6.4 physics and manual", *JHEP* **05** (2006) 026, doi:10.1088/1126-6708/2006/05/026, arXiv:hep-ph/0603175.

[19] T. Sjöstrand et al., "An Introduction to PYTHIA 8.2", *Comput. Phys. Commun.* **191** (2015) 159–177, doi:10.1016/j.cpc.2015.01.024, arXiv:1410.3012.

[20] P. Skands, S. Carrazza, and J. Rojo, "Tuning PYTHIA 8.1: the Monash 2013 Tune", *Eur. Phys. J.* **C74** (2014), no. 8, 3024, doi:10.1140/epjc/s10052-014-3024-y, arXiv:1404.5630.

[21] CMS Collaboration, "Event generator tunes obtained from underlying event and multiparton scattering measurements", *Eur. Phys. J.* **C76** (2016), no. 3, 155, doi:10.1140/epjc/s10052-016-3988-x, arXiv:1512.00815.

[22] S. Frixione, P. Nason, and C. Oleari, "Matching NLO QCD computations with Parton Shower simulations: the POWHEG method", *JHEP* **11** (2007) 070, doi:10.1088/1126-6708/2007/11/070, arXiv:0709.2092.

[23] S. Alioli et al., "A general framework for implementing NLO calculations in shower Monte Carlo programs: the POWHEG BOX", *JHEP* **06** (2010) 043, doi:10.1007/JHEP06(2010)043, arXiv:1002.2581.

[24] CMS Collaboration, "Investigations of the impact of the parton shower tuning in Pythia 8 in the modelling of $t\bar{t}$ at $\sqrt{s} = 8$ and 13 TeV", Technical Report CMS-PAS-TOP-16-021, CERN, Geneva, 2016.

[25] M. Beneke, P. Falgari, S. Klein, and C. Schwinn, "Hadronic top-quark pair production with NNLL threshold resummation", *Nucl. Phys. B* **855** (2012) 695, doi:10.1016/j.nuclphysb.2011.10.021, arXiv:1109.1536.

[26] M. Cacciari et al., "Top-pair production at hadron colliders with next-to-next-to-leading logarithmic soft-gluon resummation", *Phys. Lett. B* **710** (2012) 612, doi:10.1016/j.physletb.2012.03.013, arXiv:1111.5869.

[27] P. Bärnreuther, M. Czakon, and A. Mitov, "Percent-Level-Precision Physics at the Tevatron: Next-to-Next-to-Leading Order QCD Corrections to $q\bar{q} \to t\bar{t} + X$", *Phys. Rev. Lett.* **109** (2012) 132001, doi:10.1103/PhysRevLett.109.132001, arXiv:1204.5201.

[28] M. Czakon and A. Mitov, "NNLO corrections to top-pair production at hadron colliders: the all-fermionic scattering channels", *JHEP* **12** (2012) 054, doi:10.1007/JHEP12(2012)054, arXiv:1207.0236.

[29] M. Czakon and A. Mitov, "NNLO corrections to top pair production at hadron colliders: the quark-gluon reaction", *JHEP* **01** (2013) 080, doi:10.1007/JHEP01(2013)080, arXiv:1210.6832.

[30] M. Czakon, P. Fiedler and A. Mitov, "Total Top-Quark Pair-Production Cross Sec. at Hadron Colliders Through $O(\alpha_S^4)$", *Phys. Rev. Lett.* **110** (2013) 252004, doi:10.1103/PhysRevLett.110.252004, arXiv:1303.6254.

[31] S. Frixione and B. R. Webber, "Matching NLO QCD computations and parton shower simulations", *JHEP* **06** (2002) 029, doi:10.1088/1126-6708/2002/06/029, arXiv:hep-ph/0204244.

[32] N. Kidonakis, "Top Quark Production", in *Proceedings, Helmholtz International Summer School on Physics of Heavy Quarks and Hadrons (HQ 2013)*, pp. 139–168. 2014. arXiv:1311.0283. doi:10.3204/DESY-PROC-2013-03/Kidonakis.

[33] E. Re, "Single-top Wt-channel production matched with parton showers using the POWHEG method", *Eur. Phys. J. C* **71** (2011) 1547, doi:10.1140/epjc/s10052-011-1547-z, arXiv:1009.2450.

[34] J. M. Campbell and R. K. Ellis, "MCFM for the Tevatron and the LHC", *Nucl. Phys. Proc. Suppl.* **205-206** (2010) 10, doi:10.1016/j.nuclphysbps.2010.08.011, arXiv:1007.3492.

[35] S. Agostinelli et al., "Geant4a simulation toolkit", *Nuclear Instruments and Methods in Physics Research Sec. A: Accelerators, Spectrometers, Detectors and Associated Equipment* **506** (2003), no. 3, 250 – 303, doi:https://doi.org/10.1016/S0168-9002(03)01368-8.

[36] CMS Collaboration, "Particle-flow reconstruction and global event description with the cms detector", (2017). arXiv:1706.04965. JINST 12 (2017) no. 10, P10003.

[37] CMS Collaboration, "Jet energy scale and resolution in the CMS experiment in pp collisions at 8 TeV", *JINST* **12** (2017) P02014, doi:10.1088/1748-0221/12/02/P02014, arXiv:1607.03663.

[38] CMS Collaboration, "Performance of electron reconstruction and selection with the CMS detector in proton-proton collisions at $\sqrt{s} = 8$ TeV", *JINST* **10** (2015) P06005, doi:10.1088/1748-0221/10/06/P06005, arXiv:1502.02701.

[39] CMS Collaboration, "Performance of CMS muon reconstruction in pp collision events at $\sqrt{s} = 7$ TeV", *JINST* **7** (2012) P10002, doi:10.1088/1748-0221/7/10/P10002, arXiv:1206.4071.

[40] CMS Collaboration, "The CMS experiment at the CERN LHC", *JINST* **3** (2008) S08004, doi:10.1088/1748-0221/3/08/S08004.

[41] CMS Collaboration, "Identification of heavy-flavour jets with the CMS detector in pp collisions at 13 TeV", (2017). arXiv:1712.07158. Submitted to *JINST*.

[42] V. Khachatryan et al., "Measurement of the differential cross section for top quark pair production in pp collisions at $\sqrt{s} = 8$tev", *Eur. Phys. J. C* **75** (Nov, 2015) 542, doi:10.1140/epjc/s10052-015-3709-x.

[43] CMS Collaboration, "First measurement of the differential cross section for ttbar production in the dilepton final state at sqrts = 13 TeV", Technical Report CMS-PAS-TOP-15-010, CERN, Geneva, 2015.

[44] CDF Collaboration, "Measurement of the top quark mass using template methods on dilepton events in proton antiproton collisions at $\sqrt{s} = 1.96$-TeV.", *Phys. Rev.* **D73** (2006) 112006, doi:10.1103/PhysRevD.73.112006, arXiv:hep-ex/0602008.

[45] L. Moneta et al., "The RooStats Project", in *13th International Workshop on Advanced Computing and Analysis Techniques in Physics Research (ACAT2010)*. SISSA, 2010. arXiv:1009.1003. PoS(ACAT2010)057.

[46] J. S. Conway, "Incorporating Nuisance Parameters in Likelihoods for Multisource Spectra", in *Proceedings, PHYSTAT 2011 Workshop on Statistical Issues Related to Discovery Claims in Search Experiments and Unfolding, CERN,Geneva, Switzerland 17-20 January 2011*, pp. 115–120. 2011. arXiv:1103.0354. doi:10.5170/CERN-2011-006.115.

[47] C. G. Lester and D. J. Summers, "Measuring masses of semiinvisibly decaying particles pair produced at hadron colliders", *Phys. Lett.* **B463** (1999) 99–103, doi:10.1016/S0370-2693(99)00945-4, arXiv:hep-ph/9906349.

[48] M. Burns, K. Kong, K. T. Matchev, and M. Park, "Using Subsystem MT2 for Complete Mass Determinations in Decay Chains with Missing Energy at Hadron Colliders", *JHEP* **03** (2009) 143, doi:10.1088/1126-6708/2009/03/143, arXiv:0810.5576.

[49] H.-C. Cheng and Z. Han, "Minimal Kinematic Constraints and m(T2)", *JHEP* **12** (2008) 063, doi:10.1088/1126-6708/2008/12/063, arXiv:0810.5178.

[50] CMS Collaboration, "Search for dark matter produced in association with heavy-flavor quarks in proton-proton collisions at sqrt(s)=13 TeV", arXiv:1706.02581.

[51] A. Hoecker et al., "TMVA: Toolkit for Multivariate Data Analysis", *PoS* **ACAT** (2007) 040, arXiv:physics/0703039.

[52] CMS Collaboration, "Performance of the cms missing transverse momentum reconstruction in pp data at s = 8 tev", *Journal of Instrumentation* **10** (2015), no. 02, P02006, doi:10.1088/1748-0221/10/02/P02006.

[53] J. Butterworth et al., "Pdf4lhc recommendations for lhc run ii", *Journal of Physics G: Nuclear and Particle Physics* **43** (2016), no. 2, 023001, doi:10.1088/0954-3899/43/2/023001.

[54] CMS Collaboration, "CMS Luminosity Measurements for the 2016 Data Taking Period", Technical Report CMS-PAS-LUM-17-001, CERN, Geneva, 2017.

[55] CMS Collaboration, "Identification of b quark jets at the CMS Experiment in the LHC Run 2", Technical Report CMS-PAS-BTV-15-001, CERN, Geneva, 2016.

[56] ATLAS and CMS Collaborations, "Procedure for the LHC Higgs boson search combination in summer 2011", Technical Report ATL-PHYS-PUB-2011-011, CMS-NOTE-2011-005, CERN, 2011.

[57] T. Junk, "Confidence level computation for combining searches with small statistics", *Nucl. Instrum. Meth. A* **434** (1999) 435, doi:10.1016/S0168-9002(99)00498-2, arXiv:hep-ex/9902006.

[58] A. L. Read, "Presentation of search results: the CL_s technique", *J. Phys. G* **28** (2002) 2693, doi:10.1088/0954-3899/28/10/313.

[59] G. Cowan, K. Cranmer, E. Gross, and O. Vitells, "Asymptotic formulae for likelihood-based tests of new physics", *Eur. Phys. J. C* **71** (2011) 1554, doi:10.1140/epjc/s10052-011-1554-0, 10.1140/epjc/s10052-013-2501-z, arXiv:1007.1727. [Erratum: *Eur. Phys. J. C* **73** (2013) 2501].